2020

Vibration suppression for monopile and spar-buoy offshore wind turbines using the structure-immittance approach

Yi-Yuan Li

Semyung Park

Jason Zheng Jiang

Matthew Lackner

Simon Neild

See next page for additional authors

Authors

Yi-Yuan Li, Semyung Park, Jason Zheng Jiang, Matthew Lackner, Simon Neild, and Ian Ward

Received: 7 January 2020 | Revised: 3 April 2020 | Accepted: 19 May 2020

DOI: 10.1002/we.2544

RESEARCH ARTICLE

WILEY

Vibration suppression for monopile and spar-buoy offshore wind turbines using the structure-immittance approach

Yi-Yuan Li[1] | Semyung Park[2] | Jason Zheng Jiang[1] | Matthew Lackner[2] | Simon Neild[1] | Ian Ward[3]

[1]Department of Mechanical Engineering, University of Bristol, Bristol, UK

[2]Department of Mechanical and Industrial Engineering, University of Massachusetts Amherst, Amherst, Massachusetts, USA

[3]Infrastructure Department, SNC-Lavalin Atkins, Epsom, UK

Correspondence to:
Jason Zheng Jiang, Department of Mechanical Engineering, Queen's Building, University Walk, Bristol BS8 1TR, UK.
Email: z.jiang@bristol.ac.uk

Funding information
Atkins; China Scholarship Council; Engineering and Physical Sciences Research Council, Grant/Award Number: EP/P013546/1; University of Bristol; Deans Scholarship from the University of Bristol; China Scholarship Council; EPSRC, Grant/Award Number: EP/P013546/1; Impact Acceleration Account Award with Atkins

Peer Review
The peer review history for this article is available at https://publons.com/publon/10.1002/we.2544.

Abstract

Offshore wind turbines have the potential to capture the high-quality wind resource. However, the significant wind and wave excitations may result in excessive vibrations and decreased reliability. To reduce vibrations, passive structural control devices, such as the tuned mass damper (TMD), have been used. To further enhance the vibration suppression capability, inerter-based absorbers (IBAs) have been studied using the structure-based approach, that is, proposing specific stiffness-damping-inertance elements layouts for investigation. Such an approach has a critical limitation of being only able to cover specific IBA layouts, leaving numerous beneficial configurations not identified. This paper adopts the newly introduced structure-immittance approach, which is able to cover all network layout possibilities with a predetermined number of elements. Linear monopile and spar-buoy turbine models are first established for optimisation. Results show that the performance improvements can be up to 6.5% and 7.3% with four and six elements, respectively, compared with the TMD. Moreover, a complete set of beneficial IBA layouts with explicit element types and numbers have been obtained, which is essential for next-step real-life applications. In order to verify the effectiveness of the identified absorbers with OpenFAST, an approach has been established to integrate any IBA transfer functions. It has been shown that the performance benefits preserve under both the fatigue limit state (FLS) and the ultimate limit state (ULS). Furthermore, results show that the mass component of the optimum IBAs can be reduced by up to 25.1% (7,486 kg) to achieve the same performance as the TMD.

KEYWORDS
offshore wind turbines, passive structural control, structure-immittance approach, tower vibration mitigation

1 | INTRODUCTION

Offshore wind turbines experience significant loadings from the external metocean conditions including wind, waves, and currents, which can reduce the reliability of the turbines and ultimately increase the cost of energy.[1] Load mitigation is therefore a critical strategy to reduce

vibrations and deflections in turbine components, and thus extend lifetime and increase reliability. Passive structural control, which is appealing due to its simplicity and zero power input, is one such strategy and is employed in this paper for the vibration mitigation of offshore fixed-bottom and floating wind turbines.

The most commonly used passive structural control device is the tuned mass damper (TMD),[2,3] which has been intensively investigated for wind turbine applications. Murtagh et al[4] studied the vibration mitigation of an onshore wind turbine model by using a TMD aligned with the wind forcing. Lackner and Rotea[5] included passive TMD technology into the FAST code,[6] which is a fully coupled aero-hydro-servo-elastic code developed by the National Renewable Energy Laboratory (NREL) to simulate the loads and performance of offshore wind turbines. Later, optimum TMD parameter values were investigated based on simplified limited degree-of-freedom (DOF) turbine models[7] developed by Stewart and Lackner,[8] and the effects of wind-wave misalignment on turbines were studied.[8] Si et al[9] established a 5-DOF spar-buoy floating turbine model and investigated the vibration suppression performance of a TMD in the platform. Beyond a single passive TMD, Zuo et al[10] investigated the effect of multiple TMDs on a finite-element monopile turbine model written in ABAQUS®; Sun[11] also investigated the vibration suppression of a monopile turbine using a semiactive TMD under multi-hazards. Furthermore, Park et al[12] included a single pendulum TMD in FAST, which can oscillate omni-directionally (i.e., 2-D motion) with different semi-active control strategy.

To further enhance the vibration suppression capability of a conventional passive absorber, an additional passive mechanical element, the inerter, can be included. The inerter was first introduced by Smith.[13] It is a two-terminal device with the property that the force generated is proportional to the relative acceleration across its two terminals. With the inerter, the force-current analogy[14] between mechanical and electrical systems can be fully achieved, where the mechanical elements springs, dampers and inerters correspond to the electrical elements inductors, resistors, and capacitors, respectively. Including the inerter in the traditional passive absorber forms the inerter-based absorber (IBA), which connects a reaction mass to the main system via the layout consisting of springs, dampers and inerters. The significant performance benefits of IBAs have been obtained for multiple mechanical systems, such as automotives,[15,16] railway vehicles,[17-19] landing gears,[20] and buildings.[21] The introduction of the inerter element fundamentally enlarged the vibration suppression function ability which can be realised passively. It is worth to point out that much research attention has been spent on the physical realisation of inertance. Several approaches, for example, the ball-screw mechanism,[13,22,23] the fluid-inertance realisation,[24-26] can be pursued for wind turbine applications.

Traditionally, the structure-based approach is employed to determine the IBA layouts. With this approach, the complexity and topology of the absorber is predetermined. However, only one network layout can be considered at a time despite the fact that there are a large number of possible layouts, which inevitably limits the achievable performance of the proposed absorber. Previous investigations on IBAs for the wind turbine vibration suppression all adopted the structure-based apporach. For example, Hu et al[27] investigated the vibration mitigation for a barge type floating turbine by using three 5-element IBAs, and the IBAs were assessed in FAST under the normal operational condition with moderate wind and wave loads. Later, a 4-element IBA was investigated for the vibration suppression of an onshore wind turbine subjected to seismic loads,[28] where the ground motion is considered as the input load. More recently, the tuned-mass-damper-inerter (TMDI)[29] was considered in a spar-buoy turbine for its vibration suppression,[30] and it showed substantial performance improvements. It worth to note that TMDI requires two connection points to the turbine system, which could potentially be hard to implement in real life. Therefore, the present work only focuses on one attachment point absorbers. These structure-based studies leave a substantial number of alternative IBAs not being considered. Hence, it is difficult to decide whether the optimum IBA configurations have been obtained and if there exist alternative IBA layouts with similar or even higher performance benefits. To overcome the disadvantages of the structure-based approach, the structure-immittance approach, based on the network-synthesis theory for the passive vibration absorber identification, was proposed by Zhang et al.[31] With this approach, a new class of structural immittance functions can be obtained, which can cover a full set of network layouts with explicit information of all topology possibilities; meanwhile, the number of each element type is predetermined, and the element values can be fixed or constrained. In this study, a full range of IBA layouts with a predetermined number of elements is investigated by employing the structure-immittance approach. All beneficial IBAs containing no more than six explicit elements are identified systematically, and the identification results are compared and discussed with the structure-based IBAs where the traditional passive absorber TMD is taken as the benchmark. Then, the latest version of FAST, that is, OpenFAST,[32] is chosen as the simulation tool to assess the performance of the identified beneficial IBAs on the wind turbine dynamics. OpenFAST couples computational modules of aerodynamics, hydrodynamics for offshore structures, control and electrical system (servo) dynamics, and structural dynamics to enable coupled nonlinear aero-hydro-servo-elastic simulations in the time domain.[32] In this study, we introduce an approach to include absorber properties described by transfer functions representing their terminal behaviours into OpenFAST via the *Servo* glue code. This enables the fully exploration of the performance of a whole range of IBA configurations on any wind turbine types included in OpenFAST. Here, a fixed-bottom monopile and a floating spar-buoy platform turbine are investigated to show the performance improvements of the optimum IBAs under both normal operational and extreme loading conditions.

This paper is arranged as follows: In Section 2, monopile and spar-buoy turbine models used in OpenFAST are introduced, and their corresponding simplified linear models are identified. Then, the structure-immittance approach and optimisation procedures are briefly introduced in Section 3, with the obtained optimisation results presented. In Section 4, the identified absorbers' configurations are assessed by employing OpenFAST under both normal operational and extreme loading conditions. In order to achieve such simulations, the implementation of the IBAs' transfer functions in OpenFAST is also introduced in Section 4. Finally, conclusions are drawn in Section 5.

2 | OFFSHORE WIND TURBINE MODELS

In this work, beneficial IBA configurations are first identified using linear monopile and spar-buoy wind turbine models. The performance advantages will then be verified by using OpenFAST, a nonlinear aero-hydro-servo-elastic coupled simulation tool developed by NREL.[32] In OpenFAST, the NREL 5-MW wind turbine[33] is adopted as the default turbine model, which has been used as the reference model in a variety of wind turbine studies.[7,9-11,27] It can be modelled with different support structures, including the monopile, jacket, tripod, barge, spar-buoy, or tension-leg-platform. Throughout this study, the dynamics of a monopile and a spar-buoy turbine are investigated and the performance of passive vibration suppression systems are assessed. This assessment will be across a family of IBA layouts for a given kind of complexity in terms of component numbers. It should be noted that the optimum IBA configurations can also be identified by carrying out the optimisation within OpenFAST, but this is not computationally feasible. For example, a 10-min simulation requires around 5 min of simulation time, and to find the optimum values, thousands of function calls might be needed, with numerous candidate IBA layouts considered as well. Therefore, simplified linear models for the monopile and spar-buoy wind turbines are first established as shown in Figure 1A,B, respectively, where the absorber is considered inside the nacelle. The IBAs can be represented by a reaction mass connected to the main system with a combination of springs, dampers, and inerters. The connection is represented by a transfer function $Y(s)$, as shown in Figure 1, which is defined as the force to the relative velocity across its two terminals as follows:

$$Y(s) = \frac{F(s)}{\Delta V(s)}. \tag{1}$$

$F(s)$ is the exerted force of the IBA (output), and $\Delta V(s)$ is the associated relative change in velocities (input) between the reaction mass and the nacelle, that is, across the transfer function $Y(s)$. For example, $Y(s)=(k+cs)/s$ for the TMD, where a spring with stiffness k and a damper with damping c are connected in parallel.

2.1 | Monopile wind turbine model

The NREL 5-MW baseline wind turbine is a representative utility-scale multimegawatt turbine. It is a conventional three-bladed, upwind, variable-speed, blade-pitch-to-feather-controlled turbine. In OpenFAST, the 5-MW wind turbine is connected to a monopile which has a constant diameter of 6 m and a constant thickness of 0.060 m. The tower base begins at an elevation of 10 m above the still-water level (SWL), and the monopile extends from the tower base down to the mudline, which is 20 m below the SWL.[34]

Following the previous work,[7] a simplified linear monopile turbine model is established based on the above-stated OpenFAST monopile turbine model. The tower fore-aft bending mode is responsible for the most of the fatigue loads, hence two DOFs are considered here: the tower fore-aft bending DOF and the IBA's mass DOF. Applying the small angle approximation and considering the absorber in the noninertial reference frame, equations of motion of the system are given in Laplace domain as follows:

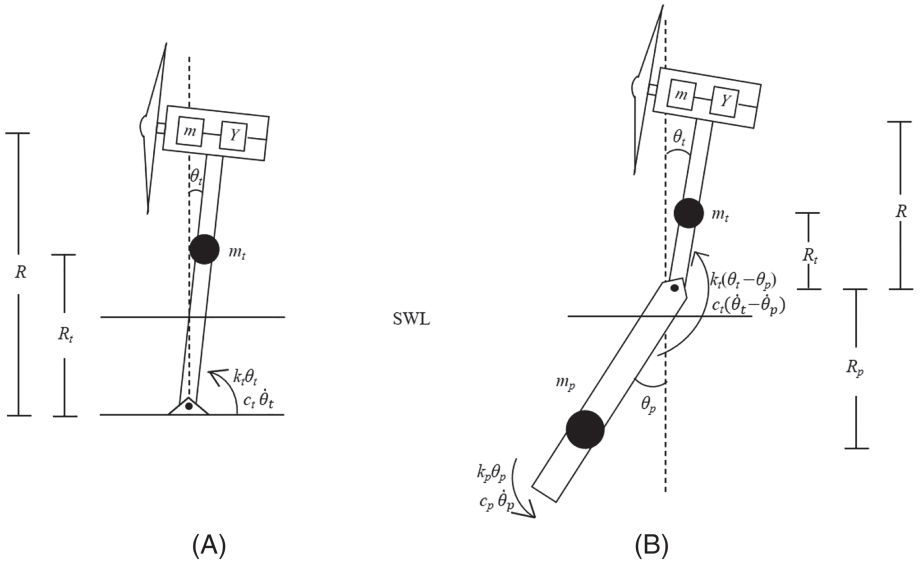

FIGURE 1 Simplified linear offshore wind turbine models[7]: (A) the monopile turbine and (B) the spar-buoy turbine

$$\begin{cases} m\tilde{x}_r(s)s^2 = & mg\tilde{\theta}_t(s) - Y(s)\tilde{x}_r(s)s - mR\tilde{\theta}_t(s)s^2 \\ I_t\tilde{\theta}_t(s)s^2 = & m_t gR_t\tilde{\theta}_t(s) + RY(s)\tilde{x}_r(s)s - (k_t + c_t s)\tilde{\theta}_t(s) + mg\tilde{x}_r(s) + M_{wind/wave}, \end{cases} \quad (2)$$

where m_t is the turbine's total mass and m is the absorber's mass. $M_{wind/wave}$ is the input wind/wave moment to the monopile turbine. The angle that the tower has deflected from vertical is denoted by θ_t. The nacelle of the OWT is considered as a reference frame and the displacement of the absorber x_r is relative to the nacelle. So, the term $mR\tilde{\theta}_t(s)s^2$ exists due to the noninertial reference frame. Note that $\tilde{\theta}_t(s)$ and $\tilde{x}_r(s)$ are the Laplace domain expression of $\theta_t(t)$ and $x_r(t)$. R and R_t are the distances from the tower hinge to the absorber's mass and the centre of the turbine total mass, respectively. k_t and c_t are the rotary stiffness and rotary damping constants at the tower base. $Y(s)$ is the representation of the transfer function of an absorber consisting of inerters, dampers, and springs as defined in equation (1). The absorber's mass m is taken to be equal to 10,000 kg, which is approximately 1% of the turbine's total mass m_t.

First, model parameters must be determined. I_t, m_t, R_t, and R can be obtained from other studies[34,35] and the OpenFAST input files, which are summarised in Table 1. The rotary stiffness k_t and the rotary damping c_t need to be determined by matching the linear model response to the OpenFAST output under the same input conditions. Here an initial condition of the tower top displacement (TTD) equal to 1 m is used in OpenFAST, which is the amount of tower bending in metres measured at the top of tower. The response of the linear model is fit to the OpenFAST output in MATLAB® by minimising the root-mean-square of the discrepancy between the OpenFAST output and the linear model response. *patternsearch* and *fminsearch* command in MATLAB® are used to identify the optimum parameter values with *fminsearch* refining the results obtained via *patternsearch*. Results of the TTD for the monopile turbine model in the time and frequency domains are shown in Figure 2A,B, respectively. The frequency domain response is obtained by applying the Fast Fourier Transform (FFT) to the time domain response. The resulting rotary stiffness and damping values are identified as k_t=1.32×10^{10} N·m/rad and c_t=2.65×10^7 N·m·s/rad, respectively. It should be noted that all the DOFs are activated in OpenFAST to make sure the modal frequencies of the OWT system are captured accurately. It can be seen from Figure 2A that there are certain discrepancies in the first 30 s. This is mainly caused by the presence of a flexible foundation in the full model (i.e., use *CompSub* in OpenFAST). In this case, the first 30 s response is omitted when fitting the simplified linear model with the OpenFAST response in order to

TABLE 1 Parameter values of the linear monopile and spar-buoy turbine models

Properties	Parameter values of monopile turbine	Parameter values of spar-buoy turbine
Total turbine mass m_t	929,397 kg	656,498 kg
Absorber's mass m	10,000 kg	10,000 kg
Tower inertia I_t	4.30×10^9 kg·m^2	2.73×10^9 kg·m^2
Platform mass m_p	/	7,466,330 kg
platform inertia I_p	/	1.54×10^{11} kg·m^2
Turbine's height to the tower hinge R	107.6 m	77.6 m
Turbine mass centre to the tower hinge R_t	67.997 m	64.5 m
Platform mass centre to the tower hinge R_p	/	-99.9155 m
Rotary stiffness of the tower k_t	1.32×10^{10} N·m/rad	2.43×10^{10} N·m/rad
Rotary damping of the tower c_t	2.65×10^7 N·m·s/rad	1.02×10^8 N·m·s/rad
Rotary stiffness of the platform k_p	/	0 N·m/rad
Rotary damping of the platform c_p	/	3.55×10^9 N·m·s/rad
Dominant mode frequencies	0.28 Hz	0.035 Hz, 0.48 Hz

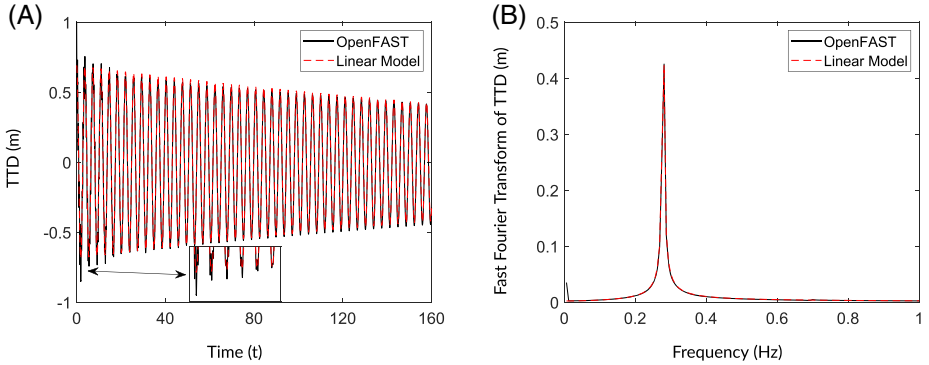

FIGURE 2 Comparison of the tower top displacement (TTD) response of the monopile turbine by employing the linear model and OpenFAST in (A) the time domain and (B) the frequency domain [Colour figure can be viewed at wileyonlinelibrary.com]

neglect the foundation dynamics. Moreover, nonzero mean responses causes the nonzero value at 0 Hz of the frequency domain response as shown in Figure 2B. This is mainly because the nacelle mass centre is not aligned with the tower mass centreline, which results in a constant moment applied to the tower base. Furthermore, it can be noted from Figure 2B that the monopile turbine oscillates at a frequency of approximately 0.28 Hz.

2.2 | Spar-buoy wind turbine model

In OpenFAST, the NREL 5-MW turbine can be coupled with a spar-buoy floating platform called "Hywind," which was originally developed by Statoil. The turbine tower is cantilevered at an elevation of 10 m above the SWL to the top of the floating platform. The length of the platform is 120 m, and its mass is centred at 89.92 m along the platform centreline below the SWL.[36] The simplified linear spar-buoy turbine model is established accordingly. Here, the tower fore-aft bending and platform pitch modes are responsible for the most of the fatigue loading. Therefore, three DOFs are of concern: the tower fore-aft bending DOF, the platform pitch DOF, and the absorber's mass DOF. Similarly, after applying the small angle approximation and considering the absorber in the noninertial reference frame, equations of motion of the spar-buoy system in the Laplace domain are as follows:

$$\begin{cases} m\tilde{x}_r(s)s^2 = mg\tilde{\theta}_t(s) - Y(s)\tilde{x}_r(s)s - mR\tilde{\theta}_t(s)s^2 \\ I_t\tilde{\theta}_t(s)s^2 = m_t g R_t\tilde{\theta}_t(s) + RY(s)\tilde{x}_r(s)s - (k_t + c_t s)(\tilde{\theta}_t(s) - \tilde{\theta}_p(s)) + mg\tilde{x}_r(s) + M_{wind} \\ I_p\tilde{\theta}_p(s)s^2 = -m_p g R_p\tilde{\theta}_p(s) + (k_t + c_t s)(\tilde{\theta}_t(s) - \tilde{\theta}_p(s)) - (k_p + c_p s)\tilde{\theta}_p(s) + M_{wave}, \end{cases} \quad (3)$$

where m_p is the mass of the platform and I_p is the inertia of the platform, $\theta_p(t)$ is the angle that the platform has rotated from vertical and $\tilde{\theta}_p(s)$ is the corresponding Laplace expression, R_p is the distance from the tower hinge to the centre of the platform mass, and k_p and c_p are the rotary stiffness and damping constants of the spar-buoy platform, which are the summation of hydrostatic and mooring line effects. All the other parameters have the same definitions as those used for the linear monopile turbine model. Note that according to the definition in OpenFAST, tower top displacement is relative to the platform coordinate system. This means that if the platform is pitched while there is no bending of the tower, then the tower top displacement is zero.

Again, the model parameters must be determined first. m_t, I_t, m_p, R, R_t, and R_p can be obtained from the definition of 5-MW spar-buoy wind turbine[36] and the OpenFAST input files. Detailed information is also summarised in Table 1. The tower and platform rotary stiffness and damping constants, k_t, c_t, k_p, and c_p are identified by fitting the response from the linear model to that from OpenFAST. In addition, the platform inertia I_p needs to be identified. This is because the inertial effect of the water must be included in I_p. The platform inertia shown in the OpenFAST input

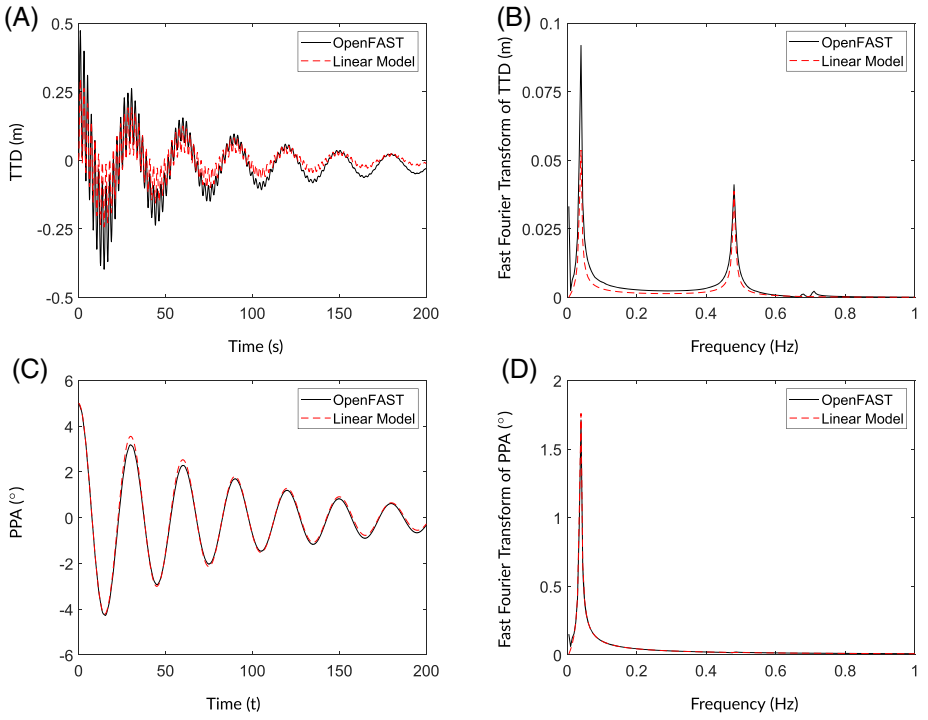

FIGURE 3 Comparison of the responses of the spar-buoy turbine by employing the linear model and OpenFAST with tower top displacement (TTD) in (A) the time domain and (B) the frequency domain and with platform pitch angle (PPA) in (C) the time domain and (D) the frequency domain [Colour figure can be viewed at wileyonlinelibrary.com]

file is the true platform inertia, whereas movement of the platform through the water will cause substantial added inertial effect, which should be considered in the simplified model. Since the added inertial effect varies little across oscillation frequency,[36] it is regarded as constant here. For the spar-buoy turbine, an initial condition of the platform pitch angle (PPA) equal to 5° is used to obtain the FAST output. Figure 3A,C shows the fitted plot for the tower top displacement and the platform pitch angle of the spar-buoy turbine. The same identification approach as the one used in the monopile turbine linear model is employed here to obtain the spar-buoy turbine parameters. Their corresponding frequency responses are shown in panels b and d. Again, since the nacelle mass centre is not along the tower and platform mass centreline, nonzero mean responses are obtained, which cause the nonzero value at 0 Hz of the frequency domain responses as shown in Figure 3B,D. Note that the fit between the simplified model and OpenFAST is not perfect. This is mainly caused by: (1) the surge and heave DOFs are important for the dynamics of the spar-buoy turbine.[9] Frequency of the heave mode is around 0.035 Hz, which is close to the platform pitch mode frequency, and hence will affect the responses. (2) The platform rotary damping constant c_p includes hydrodynamic damping, wave radiation, and viscous damping. These terms are nonlinear, so the approximated linear damping constants used in the linear model leads to discrepancies. A more accurate 5-DOF model has been developed by Si et al.[9] However, this model is not adopted here. As the passive absorbers used in this study are tuned to the system natural frequencies, optimisation results will be representative as long as the frequency of each mode of the main system is accurate. It can be seen from Figure 3B,D that the frequencies for both the platform pitch (0.035 Hz) and the tower fore-aft bending (0.48 Hz) modes are accurately captured, hence the linear spar-buoy turbine model is maintained as 2 DOFs for simplicity. The resulting rotary stiffness and damping constants of the tower and platform are k_t=2.43×10^{10} N·m/rad, c_t=1.02×10^{8} N·m·s/rad, k_p≈0 N·m/rad, and c_p=3.55×10^{9} N·m·s/rad, respectively. Identification results indicate that the platform pitch stiffness is not provided by the external rotary stiffness k_p. Instead, it is mainly provided by the gravity of the platform.

2.3 | Cost functions and constraints for the optimisation

For the monopile turbine, the tower top displacement is taken as the performance index as it is deleterious to the tower fatigue life. The objective function is defined as the H_2 norm of the transfer function from the wind/wave load input $M_{wind/wave}$ to the tower rotational angle output $\tilde{\theta}_t(s)$, denoted as $T_{M_{Wind/Wave}\to\tilde{\theta}_t(s)}$ (T stands for 'Transfer Function'), which can be obtained from equation 2. The static stiffness of IBAs is limited to be no less than the static stiffness of the TMD to constrain the maximum displacement of IBAs due to the space limitation within the turbine nacelle as follows:

$$J = ||T_{M_{Wind/Wave}\to\tilde{\theta}_t(s)}||_2 \text{where} (Y_{IBA}(s)\times s)_{s\to 0} \geqslant (\mathrm{Y_{TMD}(s)\times s})_{s\to 0}. \tag{4}$$

The H_2 norm of the transfer function represents the root-mean-squares of the impulse response of a linear dynamic system. $Y_{TMD}(s)$ and $Y_{IBA}(s)$ represent the transfer functions of the TMD and the IBA, respectively, from the relative terminal velocity to the force across the devices. Therefore, $(Y_{TMD}(s)\times s)_{s\to 0}$ and $(Y_{IBA}(s)\times s)_{s\to 0}$ represent the static stiffness of the TMD and the IBA, respectively. In the previous study,[7] the maximum strokes for the TMD have been pointed out: ±8 m in the fore-aft direction, and ±2.5 m in the side-side direction. These have been adopted as constraints for the IBAs in this study.

For the spar-buoy turbine, since there are two independent outputs for the main system (i.e., $\tilde{\theta}_t(s)$ and $\tilde{\theta}_p(s)$) and two inputs to the main system (i.e., M_{Wind} and M_{Wave}), it is a multi-input-multi-output (MIMO) system. Moreover, depending on the definition in OpenFAST, the tower top displacement is the tower top movement relative to the platform movement (i.e., $(\tilde{\theta}_t(s)-\tilde{\theta}_p(s))$). Hence, six transfer functions, $T_{M_{Wind}\to\tilde{\theta}_t(s)}$, $T_{M_{Wave}\to\tilde{\theta}_t(s)}$, $T_{M_{Wind}\to\tilde{\theta}_p(s)}$, $T_{M_{Wave}\to\tilde{\theta}_p(s)}$, $T_{M_{Wind}\to(\tilde{\theta}_t(s)-\tilde{\theta}_p(s))}$, and $T_{M_{Wave}\to(\tilde{\theta}_t(s)-\tilde{\theta}_p(s))}$, are derived as shown in Figure 4, where no device is deployed. Since the tower base bending moment is crucial to the tower fatigue life, the tower top displacement is taken as the performance index, and the objective function is defined as follows:

$$J = ||T_{M_{Wind}\to(\tilde{\theta}_t(s)-\tilde{\theta}_p(s))}||_2 + ||T_{M_{Wave}\to(\tilde{\theta}_t(s)-\tilde{\theta}_p(s))}||_2 \text{where} (Y_{IBA}(s)\times s)_{s\to 0} \geqslant (\mathrm{Y_{TMD}(s)\times s})_{s\to 0}, \tag{5}$$

which is the sum of H_2 norm of transfer functions from wind and wave load inputs to the tower relative rotational angle with the same static stiffness constraints as the one used for the monopile turbine. In this study, objective functions are optimised using a combination of *patternsearch* and *fminsearch* in MATLAB® with *fminsearch* refining the results obtained via *patternsearch*.

3 | IDENTIFICATION OF BENEFICIAL INERTER-BASED ABSORBER CONFIGURATIONS

In this section, the structure-immittance approach and the optimisation procedure are introduced to identify the beneficial IBA configurations based on the established linear turbine models and using MATLAB® optimisation commands. All beneficial IBA layouts among a full set of IBA

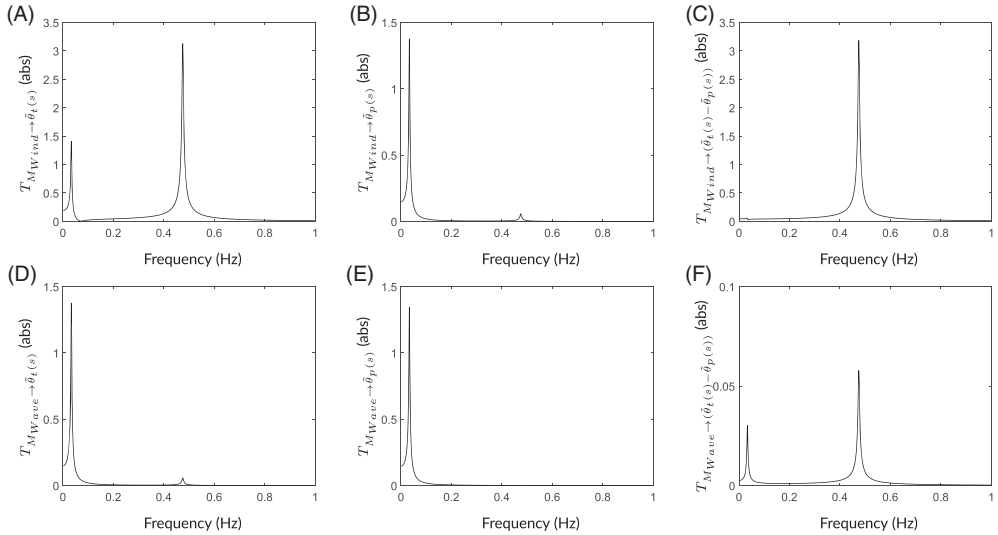

FIGURE 4 Transfer functions of the spar-buoy turbine tower absolute rotate angle ($\tilde{\theta}_t(s)$), platform absolute rotate angle ($\tilde{\theta}_p(s)$), and tower relative rotate angle ($\tilde{\theta}_t(s)-\tilde{\theta}_p(s)$) with respect to the wind input (i.e., A, B, and C) and the wave input (i.e., D, E, and F)

candidates are identified. The identification results are compared with the previously proposed structure-based IBAs, by taking the conventional vibration absorber, the TMD, as benchmark.

3.1 | Structure-immittance approach

The structure-immittance approach was first proposed by Zhang et al[31] for passive vibration absorber identification. This approach can cover a full set of network layouts with explicit information of all topology possibilities. In addition, the number of each element type can be predetermined, and element values can also be fixed or constrained. The structure-immittance approach is based on the force-current analogy,[14] where one-port (two-terminal) networks are considered. Therefore, it can be applied both on mechanical and electrical networks. By using the structure-immittance approach, generic networks which contain explicit information of all topology possibilities for a given number of each component are first constructed. Then, their corresponding mathematical expression, the structural-immittances, are derived, which are the transfer functions of the generic networks. Then, combined with the specific constraints, the structural-immittances can be used to identify the optimum IBAs among a whole range of IBA candidates in a systematic and neat way. For simplicity, detailed steps to obtain the generic networks and their corresponding structural-immittances are not stated here, instead the results of an example including two springs, one damper, and one inerter are demonstrated.

For the case of two springs, one damper, and one inerter, a total of 18 possible absorber layouts exist. By using the structure-immittance approach, two generic networks, termed Q_1 and Q_2 (see Figure 5), that contain the topology of all of these can be obtained. It should be noted that, at most, two of the springs are present for any layouts derived from the generic networks Q_1 and Q_2.

The corresponding structural-immittances of networks Q_1 and Q_2 are as follows:

$$Y_i(s) = \frac{n_i(s)}{m_i(s)} \quad (i = 1,2), \tag{6}$$

where

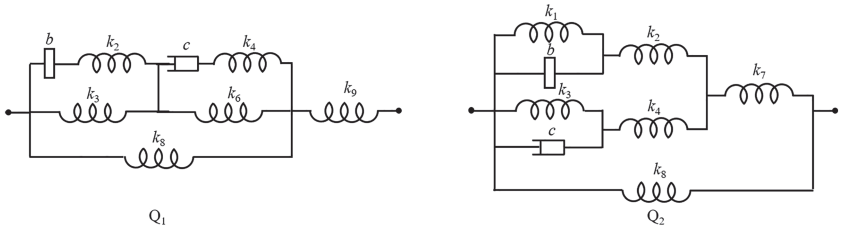

FIGURE 5 Generic networks of the two springs, one damper, and one inerter case developed by the structure-immittance approach

$$
\begin{aligned}
n_1(s) = \;& bc(k_3/k_2 + k_8/k_2 + k_6/k_4 + k_8/k_4 + 1)s^3 + b(k_6 + k_8)s^2 + \\
& c(k_3 + k_8)s + k_3k_6 + k_3k_8 + k_6k_8, \\
m_1(s) = \;& s\big(bc(1/k_2 + 1/k_4 + 1/k_9)s^3 + b(k_3/k_2 + k_6/k_2 + k_6/k_9 + k_8/k_9 + 1)s^2 + \big) \\
& (c(k_3/k_4 + k_3/k_9 + k_6/k_4 + k_8/k_9 + 1)s + k_3 + k_6), \\
n_2(s) = \;& bc(1/k_2 + 1/k_4)s^3 + b(k_3/k_2 + k_3/k_4 + k_8/k_2 + k_8/k_7 + 1)s^2 + \\
& c(k_1/k_2 + k_8/k_4 + k_1/k_4 + k_8/k_7 + 1)s + k_1 + k_3 + k_8, \\
m_2(s) = \;& s\big(bc(1/(k_2k_4) + 1/(k_2k_7) + 1/(k_4k_7))s^3 + b(1/k_2 + 1/k_7)s^2 + \big) \\
& (c(1/k_4 + 1/k_7)s + k_1/k_2 + k_1/k_7 + k_3/k_4 + k_3/k_7 + 1).
\end{aligned} \tag{7}
$$

$Y_1(s)$ and $Y_2(s)$ include all the possible combinations of two springs, one damper and one inerter. For $Y_1(s)$, only two of $1/k_2$, k_3, $1/k_4$, k_6, k_8, and $1/k_9$ are positive and all the others are equal to zero. For $Y_2(s)$, only two of k_1, $1/k_2$, k_3, $1/k_4$, $1/k_7$, and k_8 are positive and all the others are equal to zero—we refer to this as the specific constraints. These transfer functions can be used to identify the optimal IBA configurations containing two springs, one damper, and one inerter for a given system and objective functions, along with the specific constraints on the number of spring elements.

In this study, optimisations are conducted in the frequency domain. The absorber's mass is taken as 10,000 kg for both the TMD and IBA. By employing the structure-immittance approach,[31] IBAs with no more than six explicit elements are considered for both the monopile and spar-buoy turbines. For 3-element IBAs, all one spring, one damper, and one inerter combinations (totally two generic networks covering eight layouts) are considered; 4-element IBAs with all two springs, one damper, and one inerter (totally two generic networks covering 18 layouts) are considered; IBAs with two springs, two dampers, and one inerter are considered as the 5-element case (totally eight generic networks covering 79 layouts); finally 6-element IBAs consider a certain range of three springs, one damper, and two inerters (regarded as one spring paralleled to all two springs, one damper, and two inerters case (totally eight generic networks covering 79 layouts).

3.2 | Beneficial configurations for offshore wind turbines vibration suppression

Using the objective functions defined in equations 4 and 5 for the monopile and spar-buoy turbine models, respectively, the IBAs with no more than six elements are investigated by employing the structure-immittance approach.

3.2.1 | Beneficial absorber configurations with no more than 4 elements

For IBAs containing three elements or less, optimisation results show that there is no further improvements can be obtained compared with the TMD. For IBAs containing four elements (two springs, one damper, and one inerter), IBA_{4E1} is obtained for both the monopile and spar-buoy turbines, with its layouts shown in Figure 6. Optimisation results and its parameter values are shown in Tables 2 and 3correspondingly, with the TMD as a benchmark. Here, as the full range of 4-element layouts are considered, we found that IBA_{4E2}, IBA_{4E3}, and IBA_{4E4} can provide the same performance improvement (i.e., 6.5% and 5.8% for the monopile and spar-buoy turbines, respectively) as the IBA_{4E1}. This indicates that, with more beneficial IBA layouts identified by using the structure-immittance approach, wider design choices to realise the IBA can be obtained for its practical applications. We also notice that the IBA_{4E2} is the layout proposed in the previous study[28] on wind turbine vibration suppression, which serves as an evidence for the fact that the IBA layouts obtained by the structure-based approach can be regarded as a subset of the ones obtained through the structure-immittance approach. For simplicity, parameter values of the IBA_{4E2}, IBA_{4E3}, and IBA_{4E4} are not displayed here. It is worth

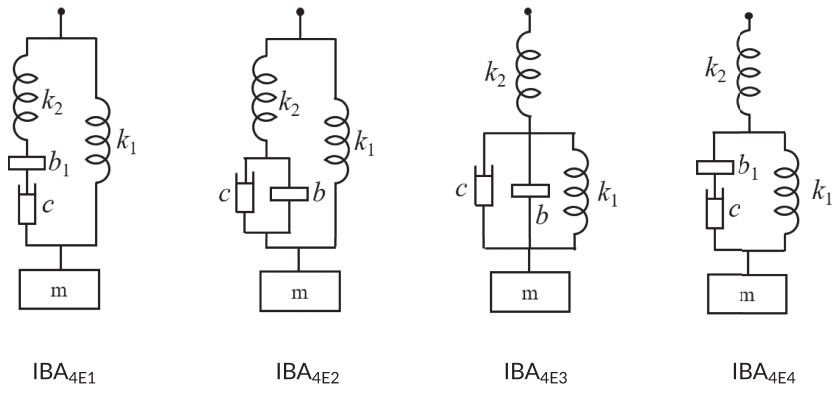

FIGURE 6 The identified beneficial 4-element inerter-based absorber (IBA) layouts with same performance improvements (i.e., 6.5% for the monopile turbine and 5.8% for the spar-buoy turbine) by employing the structure-immittance approach

TABLE 2 Optimisation results for the linear monopile turbine model

Vibration absorber	Mass value (kg)	J	Improvement	k_1 (kN/m)	k_2 (kN/m)	k_3 (kN/m)	c(kNm/s)	b_1 (kg)	b_2 (kg)
TMD	10,000	0.248	/	28.1	/	/	2.81	/	/
IBA_{4E1}	10,000	0.232	6.5%	28.3	1.64	/	3.26	563.4	/
IBA_{6E1}	10,000	0.230	7.3%	28.3	1.05	0.081	0.126	27.8	345.2

Abbreviations: IBA, inerter-based absorber; TMD, tuned mass damper.

TABLE 3 Optimisation results for the linear spar-buoy turbine model

Vibration absorber	Mass value (kg)	J	Improvement	k_1 (kN/m)	k_2 (kN/m)	k_3 (kN/m)	c(kNm/s)	b_1 (kg)	b_2 (kg)
TMD	10,000	0.173	/	86.1	/	/	4.35	/	/
IBA_{4E1}	10,000	0.163	5.8%	86.6	3.96	/	5.09	447.5	/
IBA_{6E3}	10,000	0.162	6.4%	85.7	3.43	1.91	4.53	145	421.7

Abbreviations: IBA, inerter-based absorber; TMD, tuned mass damper.

mentioning that the IBA_{4E1} and IBA_{4E2} are topologically equivalent to the two piezoelectric proof-mass absorbers studied by Høgsberg,[37] where similar level of improvements compared with TMD have been reported.

Frequency response plots of the tower top motion with the TMD and the beneficial IBAs employed for the monopile and spar-buoy turbines are shown in Figures 7 and 8, respectively. Tower top responses without an absorber included are also shown as the baseline (black dashed line) in Figures 7 and 8. The response without an absorber highlights the effectiveness of employing passive vibration absorbers. Note that the aim of this study is to improve the performance of the traditional passive vibration absorber TMD; therefore, all improvements obtained in this paper are compared with the TMD rather than the case without an absorber. It can be observed that the frequency of the tower fore-aft mode is split into two peaks by the TMD, where its natural frequency is 0.265 Hz. IBA_{4E1} have further split the tower fore-aft mode into three peaks. Natural frequencies of it are 0.245 and 0.296 Hz. Similarly for the spar-buoy turbine, the TMD and the IBA_{4E1} have split the tower fore-aft mode into two and three peaks, respectively, with natural frequency of the TMD as 0.467 Hz, of the IBA_{4E1} as 0.433 and 0.512 Hz. It should be noted that, unlike the results provided by Den Hartog[3] and Krenk,[38] the tuned two peaks by employing the TMD are not entirely flat. This is because, for the classical Den Hartog tuning approach and the relatively new equal modal damping concept proposed by Krenk, the objective is to minimise the H_{inf} norm of the system responses in the frequency domain. This is achieved by setting the dynamic amplification at two specific frequencies equal. In contrast, this study adopts the H_2 norm of the system responses as the objective function, as the H_2 norm is more relevant to the damage equivalent fatigue load. Therefore, the dynamic amplifications at these two specific frequencies does not have to be equal anymore.

3.2.2 | Beneficial absorber configurations with five and six elements

For IBAs with five elements (two springs, two dampers, and one inerter), it shows that the 5-element IBAs always reduce to 4-element IBAs with one damper not functioning for no matter the monopile or the spar-buoy offshore wind turbines. Therefore, performance improvements provided

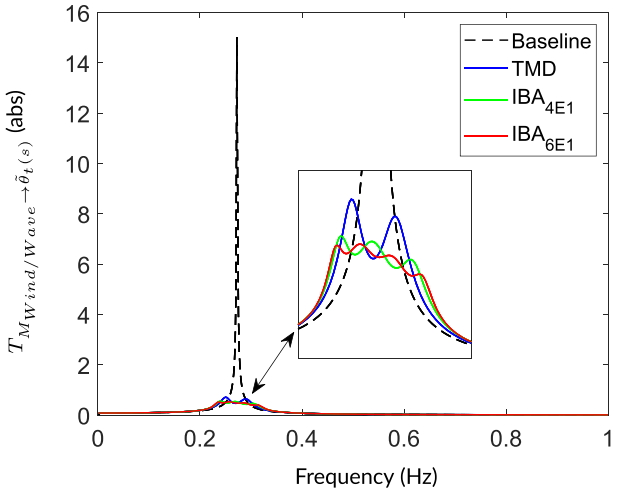

FIGURE 7 Transfer function plots of the monopile turbine tower rotational angle $\tilde{\theta}_t(s)$ with respect to the wind/wave input considering the baseline, tuned mass damper (TMD), IBA_{4E1}, and IBA_{6E1} [Colour figure can be viewed at wileyonlinelibrary.com]

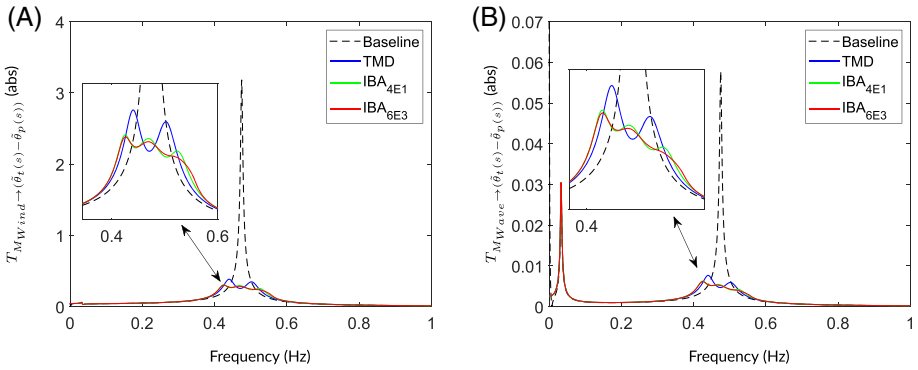

FIGURE 8 Transfer function plots of the spar-buoy turbine tower relative rotational angle ($\tilde{\theta}_t(s)-\tilde{\theta}_p(s)$) considering the baseline, tuned mass damper (TMD), IBA_{4E1}, and IBA_{6E3} with respect to (A) the wind input and (B) the wave input [Colour figure can be viewed at wileyonlinelibrary.com]

by the 5-element IBAs as shown in Hu et al,[27] all can be replaced by 4-element IBAs. For 6-element IBA layouts, a certain range of three springs, one damper, and two inerters combinations is considered (considered as one spring paralleled to all two springs, one damper, and two inerters case). Employing the structure-immittance approach, beneficial IBAs with the same performance improvements (i.e., 7.3% and 6.5% for the monopile and spar-buoy turbines, respectively) are obtained. Their layouts are shown in Figure 9, with IBA_{6E1} and IBA_{6E2} for the monopile turbine and IBA_{6E3} and IBA_{6E4} for the spar-buoy turbine. Optimisation results are also shown in Tables 2 and 3 for the monopile and spar-buoy, respectively, where only the IBA_{6E1} and IBA_{6E3} are displayed for simplicity.

Again, frequency response plots of the monopile and spar-buoy turbines tower top motion with the IBA_{6E1} and IBA_{6E3} are shown in Figures 7 and 8, respectively. It can be seen that the tower fore-aft mode of the monopile turbine is further split into four peaks by the IBA_{6E1} with its natural frequencies at 0.238, 0.272, and 0.311 Hz. Similarly, the tower fore-aft mode of the spar-buoy turbine is also split by IBA_{6E3} to four peaks with natural frequencies at 0.432, 0.510, and 0.556 Hz. Therefore, we can conclude that with extra-introduced DOFs within the absorber, the IBAs have the ability of further tuning a specific mode of the main system, and a trade-off between the elements number and performance improvement will have to be made.

To view the significance of these improvements, the mass value reductions of the identified IBAs to achieve the same performance as the TMD are now considered. In general, the performance improvements will increase as the IBAs' mass increases. However, diminishing returns can be seen in this trend, as shown in Figure 10. Figure 10A,B shows the relationships between the performance index J and the optimum IBAs mass values for the monopile and spar-buoy turbines, respectively. The absorber's mass value varies from 0 kg to 20,000 kg. Results show that the mass value of the IBA_{6E1} for the monopile turbine can be reduced by 25.1% (i.e., 7486 kg) to achieve the same performance as the TMD—this requires an optimum stiffness of k_1 = 21.3 kN/m, k_2 = 0.123 kN/m, and k_3 = 0.795 kN/m, damping of c = 0.101 kNm/s, and inertance of b_1 = 40.3 kg, b_2 = 257.7 kg. The mass value of the the IBA_{6E3} required for the spar-buoy turbine in order to achieve the same performance as the TMD is 23.2% (i.e., 7,680 kg) lower. The resulting optimum parameter values are k_1 = 66.3 kN/m, k_2 = 6.00 kN/m, k_3 = 2.62 kN/m, c = 3.49 kNm/s, and inertance b_1 = 157.2 kg, b_2 = 312.0 kg.

4 | PERFORMANCE ASSESSMENT IN REALISTIC METOCEAN EXTERNAL CONDITIONS

The above-mentioned optimisations are all based on the simplified linear turbine models. To show the performance improvements of the IBAs for the vibration mitigation of offshore wind turbines, it is necessary to verify the obtained optimisation results in OpenFAST, where more realistic

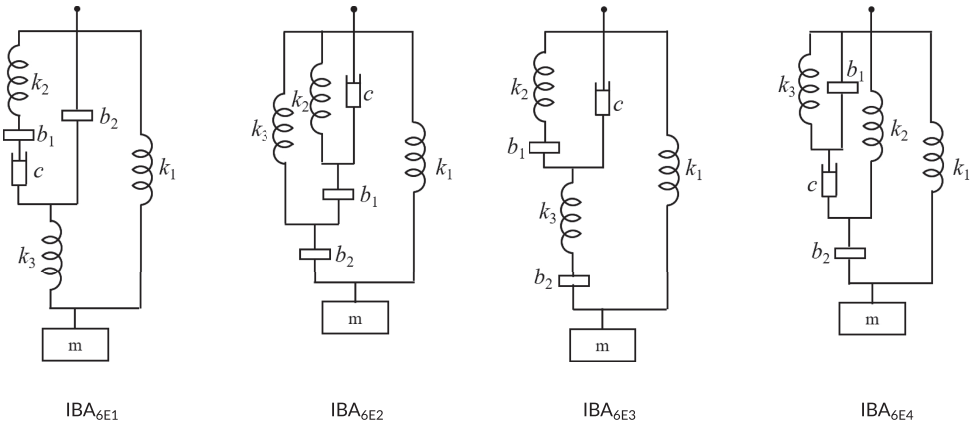

FIGURE 9 The identified beneficial 6-element inerter-based absorber (IBA) layouts with the same performance improvements (i.e., 7.3% for the monopile turbine and 6.4% for the spar-buoy turbine) by employing the structure-immittance approach

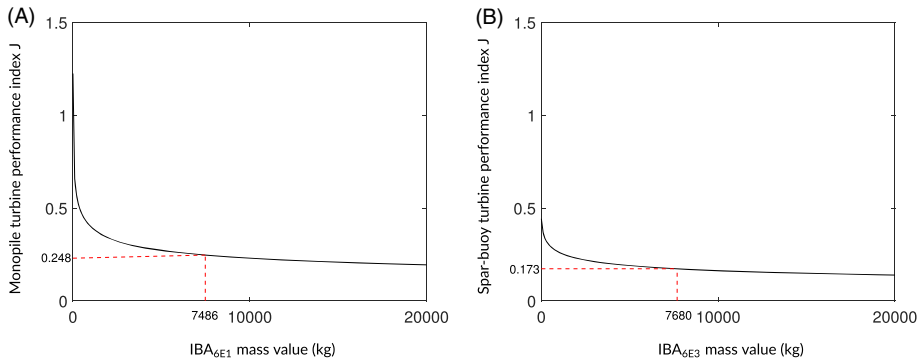

FIGURE 10 Relationships between the optimum inerter-based absorbers' (IBAs') mass values and the turbine performance index J of (A) the monopile turbine; (B) the spar-buoy turbine, where the mass reductions are 7,486 and 7,680 kg for the IBA$_{\delta E1}$ and IBA$_{\delta E3}$, respectively, to achieve the same performance as the tuned mass damper (TMD) with 10,000 kg mass value [Colour figure can be viewed at wileyonlinelibrary.com]

models can be used with representative wind and wave loading considered. First, the source code of OpenFAST is modified to allow the fully exploration of the performance of a whole range of IBAs, which is described by the transfer functions representing its two-terminal properties. Then, simulations are conducted in OpenFAST under normal operational and extreme conditions for offshore wind turbines supported by the monopile and the spar-buoy platform. For the normal operational and the extreme conditions, fatigue limit state (FLS) and ultimate limit state (ULS) are considered, respectively.

4.1 | Implementation of IBAs in OpenFAST

In order to implement structural control techniques in offshore wind turbines, two independent, single-DOF TMD systems are incorporated in FASTv7 by Lackner and Rotea,[5] named "FAST-SC." The new version source code, OpenFAST, allows for a modular approach to model the turbine dynamics, and thus an additional TMD module has been coupled to the original code. Unlike the previous version of FAST-SC (one-dimension motion), the new TMD module in OpenFAST is capable of modelling either two independent, single-DOF TMDs that can oscillate in their respective direction, or a single-pendulum TMD that can oscillate in two dimensions. The pendulum TMD modelled in the TMD module can be utilised as a passive device with constant parameters or semiactively in which the damping force can be controlled.[12] In this study, the TMD module in OpenFAST is modified in order to include all potential IBAs, where the modified module is named as the IBA module. Note that only the two independent, single-DOF IBA systems are modified to include the IBAs so far.

Based on the property of an IBA, $Y'(s)$ is defined as the transfer function from force to acceleration as follows:

$$Y'(s) = \frac{Y(s)}{s} = \frac{F(s)}{\Delta a(s)}. \tag{8}$$

For a passive absorber, $Y'(s)$ is always positive-real,[39] hence it can be written as one of the nonunique canonical state-space form as follows:

$$Y'(s) = \mathbf{c}_1(s\mathbf{I} - \mathbf{A}_1)^{-1}\mathbf{b}_1 + d_1, \tag{9}$$

where $\mathbf{A}_1 \in \mathbb{R}^{N\times N}$, $\mathbf{b}_1 \in \mathbb{R}^{N\times 1}$, $\mathbf{c}_1 \in \mathbb{R}^{1\times N}$, and d_1 are the states, inputs, outputs, and feed-forwards, respectively. N is the dimension of the internal states $\boldsymbol{\omega}_f$ (i.e., internal DOFs) of IBAs. These internal states $\boldsymbol{\omega}_f \in \mathbb{R}^{N\times 1}$ and output force F_f of $Y'(s)$ can be represented as follows:

$$\dot{\boldsymbol{\omega}}_f = \mathbf{A}_1\boldsymbol{\omega}_f + \mathbf{b}_1\ddot{x}, \tag{10}$$

$$F_f = \mathbf{c}_1\boldsymbol{\omega}_f + d_1\ddot{x}. \tag{11}$$

x is the displacement of the absorber's mass m, therefore $\ddot{x}$ is the corresponding acceleration, which is also the relative acceleration Δa across the network's two terminals, hence the IBA system input. A derivative of the force can be obtained by substituting equation (10) into equation (11) as follows:

$$\begin{aligned}\dot{F}_f &= \mathbf{c}_1\dot{\boldsymbol{\omega}}_f + d_1\dddot{x} \\ &= \mathbf{c}_1(\mathbf{A}_1\boldsymbol{\omega}_f + \mathbf{b}_1\ddot{x}) + d_1\dddot{x}.\end{aligned} \tag{12}$$

Combining the IBA's mass states with its ficitious states ω_f, the entire IBA system can be rewritten in state-space form in the time domain. Transfer functions of different IBAs can then be included in OpenFAST. A detailed procedure is shown in Appendix A. Then, results of the absorber's mass movements simulated by the IBA module are compared with the responses from MATLAB with a constant force applied. Here, only the displacement and velocity of the IBA_{6E1} are shown in Figure 11 for simplicity. It can be obtained that the responses simulated by the IBA module are the same as the ones from MATLAB, which justifies the implementation procedure. Note that the simulation is valid only when the absorber has all zero initial conditions as stated in Appendix A, which is most of the case where the absorber starts to move from the rest.

4.2 | Assessment of the monopile turbine response in realistic metocean conditions

An investigation of the impact of the TMD and IBAs for the monopile turbine is conducted by considering a set of FLS and ULS design load cases (DLCs). The DLCs are chosen based on the data gathered from the Dutch North Sea,[40] where the relevant design parameters and methods within the design basis are taken from the IEC-61400-3 standard.[41] Conditions for the FLS and ULS analysis are defined by DLC 1.2 and 6.1a, respectively. Detailed information can be found in Table 4. The FLS analysis models normal power production conditions of the offshore wind turbines with mean wind speed varies from 4 to 24 m/s with bins of 4 m/s. Each simulation lasts 660 s with the first 60 s omitted[42] to guarantee the generator torque and the blade pitch motion are in their normal operational states. The ULS cases model extreme conditions such as storms that occur rarely, but may cause failure of the structure. Under extreme conditions, the wind turbine rotor is shutdown, and the blades are pitched to feather. The simulation time is 1 h for extreme load conditions. For the monopile turbine, the water depth is considered as 20 m.

4.2.1 | Monopile turbine FLS analysis

By applying the external condition of DLC 1.2 listed in Table 4, FLS analysis results of the monopile turbine are obtained and shown in Table 5. Mlife[43] is employed to calculate the damage equivalent loads (DELs). Since the wind turbine does not experience an equal amount of time for each wind speed in practice, performance indices in this paper are weighted according to the Weibull distribution based on the UpWind Project.[40] An example result for the monopile turbine responses at a 16 m/s wind speed are illustrated in Figure 12. Here, the power spectral density (PSD) of the tower top responses in the fore-aft and side-to-side directions are shown in Figure 12A,D, which are calculated by the *pwelch* function in MATLAB with the window number chosen as 8. Corresponding time domain responses are shown in Figure 12B,E. Narrowed time domain

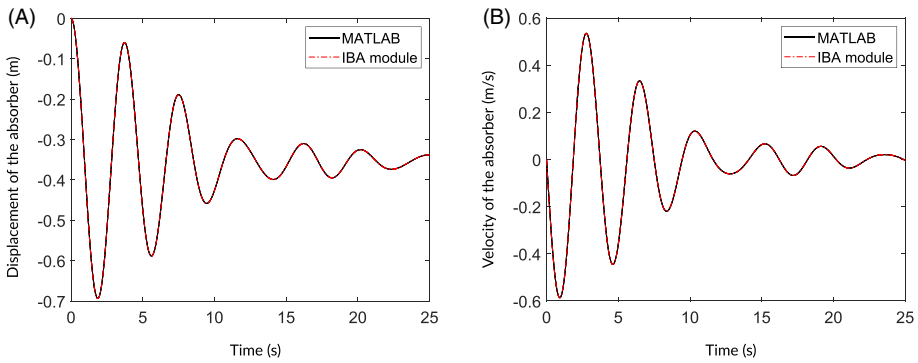

FIGURE 11 Responses of the IBA_{6E1} under a constant force input (A) the displacement amd (B) the velocity [Colour figure can be viewed at wileyonlinelibrary.com]

TABLE 4 External conditions of DLC 1.2 (FLS) and DLC 6.1a (ULS)

DLC	Wind speed (m/s)	Turb. Int. (%)	Blade pitch angle (°)	Wave height (m)	Peak period (s)	Percentage time per year (%)
	4	20.4	0	1.10	5.88	11.90
	8	16.0	0	1.31	5.67	16.48
1.2	12	14.6	3.83	1.70	5.88	12.29
(FLS)	16	13.9	12.06	2.19	6.37	5.86
	20	13.4	17.47	2.76	6.99	1.88
	24	13.1	22.35	3.42	7.80	0.41
6.1a (ULS)	41.5	11.7	90	4.9	9.43	0.003

Abbreviations: DLC, design load case; FLS, fatigue limit state; ULS, ultimate limit state.

TABLE 5 Monopile turbine FLS analysis results

	Fore-aft tower base fatigue load (kNm)		Side-to-side tower base fatigue load (kNm)			
Wind speed	TMD	IBA_{4E1}	IBA_{6E1}	TMD	IBA_{4E1}	IBA_{6E1}
4	2,575	2,525	2,523	106.0	102.0	101.8
8	7,790	7,714	7,713	718.0	681.9	679.4
12	12,896	12,809	12,810	754.6	713.6	710.8
16	13,833	13,671	13,660	1,447	1,359	1,350
20	26,170	26,013	26,018	1,754	1,656	1,646
24	19,008	18,686	18,664	4,122	3,914	3,894
Aggregated	455,475	451,173	451,090	35,834	33,904	33,748
Improvements	-	0.9%	1.0%	-	5.4%	5.8%

Abbreviations: FLS, fatigue limit state; IBA, inerter-based absorber; TMD, tuned mass damper.

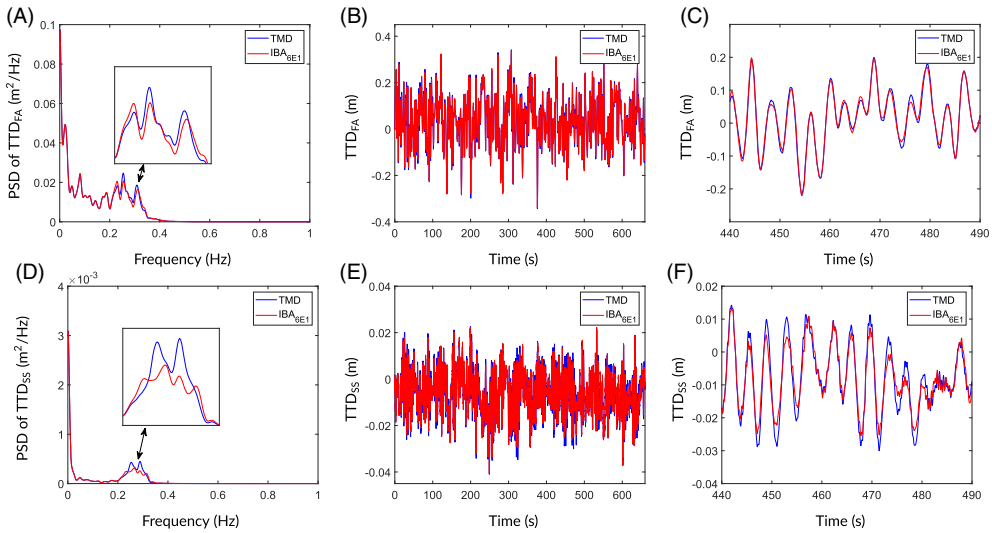

FIGURE 12 Frequency domain responses (left), time domain responses (middle), and narrowed time windows responses (right) of the monopile turbine tower top displacement (TTD) under the DLC 1.2 (16 m/s wind speed) in the fore-aft (FA) direction (A, B, C) and in the side-to-side (SS) direction (D, E, F) [Colour figure can be viewed at wileyonlinelibrary.com]

responses are also shown in Figure 12C,F. Since the performance difference between the IBA_{4E1} and IBA_{6E1} are not significant, only the responses with the TMD and IBA_{6E1} are shown. It can be seen that the IBA_{6E1} has the ability to further suppress the mode of the monopile turbine at around 0.3 Hz, which is the natural frequency of the tower fore-aft and side-to-side bending modes. IBA_{4E1} can reduce the DELs by 0.9% and 5.4% in the fore-aft and side-to-side direction, respectively, compared with the TMD. IBA_{6E1} can further reduce the DELs by 1.0% and 5.8%.

Results show that IBAs are more effective in the side-to-side direction, which is thought to be because there is less aerodynamic damping in this direction. The absorber stroke is also assessed under the FLS analysis. For the TMD, the maximum stroke for wind speeds under 24m/s is 2.38 m in the fore-aft direction and 0.55 m in the side-to-side direction. While for the IBA_{4E1} and IBA_{6E1}, the maximum stroke is 2.82 and 2.94 m in the fore-aft direction and 0.68 and 0.68 m in the side-to-side direction, respectively. It can be seen that by limiting the static stiffness of the IBAs, even though strokes of the IBAs are slightly larger than the TMD, they are still within the space limits of the turbine nacelle. Moreover, the mass optimisation obtained from Section 3.3 is also verified in OpenFAST. Results show that, with a reduced mass value of 7,486 kg, the IBA_{6E1} can provide similar performance as the optimum TMD with a 10,000-kg mass in both the fore-aft and the side-to-side direction. Therefore, the identified IBA is potentially beneficial for the offshore wind turbine applications in practice.

4.2.2 | Monopile turbine ULS analysis

Simulations subjected to the DLC 6.1a are performed for the optimised TMD and IBAs, where performance metrics are defined as the absolute maximum tower top displacement and tower base bending moment of each simulation averaged over six different random simulations. The amplitude of the tower top displacement and tower base bending moment in the frequency domain (around 0.2-0.4 Hz) are also included in Figure 13 for comparison. Results are shown in Table 6. It can be observed that the IBAs can reduce the maximum tower bending moment by up to 2.4% and 1.4% in the fore-aft and side-to-side directions, respectively. Moreover, the amplitude reduction of the tower bending mode in the frequency

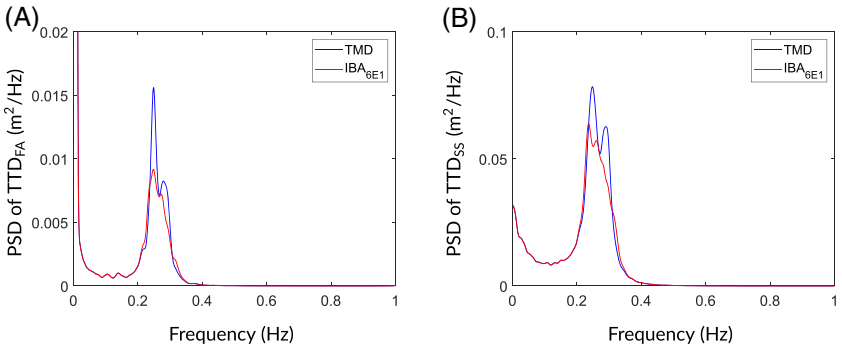

FIGURE 13 Frequency domain responses of the monopile turbine tower top displacements (TTD) under DLC 6.1a (A) in the fore-aft (FA) direction and (B) in the side-to-side (SS) direction [Colour figure can be viewed at wileyonlinelibrary.com]

TABLE 6 Monopile turbine ULS analysis results

Evaluation type	Evaluation index	TMD	IBA$_{4E1}$ (Imp.)	IBA$_{6E1}$ (Imp.)
	Max TTD fore-aft (m)	0.284	0.275 (3.0%)	0.274 (3.4%)
	Max TTD side-side (m)	0.551	0.546 (0.9%)	0.543 (1.4%)
Time domain responses				
	Max tower bending moment fore-aft (kN·m)	50,323	49,122 (2.4%)	49,159 (2.3%)
	Max tower bending moment side-side (kN·m)	86,084	85,262 (1.0%)	84,880 (1.4%)
	Amplitude TTD fore-aft (m^2/Hz)	0.0144	0.0092 (36.3%)	0.0090 (37.2%)
PSD of the responses	Amplitude TTD side-side (m^2/Hz)	0.0878	0.0673 (23.4%)	0.0638 (27.4%)
(between 0.2 and 0.4 Hz)	Amplitude tower bending moment fore-aft ((kN·m)^2/Hz)	3.52×10^8	2.25×10^8 (36.1%)	2.22×10^8 (37.0%)
	Amplitude tower bending moment side-side ((kN·m)^2/Hz)	2.15×10^9	1.64×10^9 (23.5%)	1.56×10^9 (27.4%)

Abbreviations: IBA, inerter-based absorber; TMD, tuned mass damper; TTD, tower top displacement; ULS, ultimate limit state.

domain is more significant, which can be up to 37.0% and 27.4% in the fore-aft and side-to-side directions, respectively. The PSDy of one of the ULS simulation results is shown in Figure 13A,B via *pwelch* with 36 windows. It can be observed that both IBAs are effective in suppressing the tower bending mode, around 0.28 Hz, under the extreme load case. As the blades are all feathered, drag forces and aerodynamic damping become larger in the side-to-side direction. This explains why the performance is better in the fore-aft direction while the absolute values are larger in the side-to-side direction, which is contrast to the situation under normal operational conditions.

4.3 | Assessment of the spar-buoy turbine response in realistic metocean conditions

The impact of the optimised TMD and IBAs under FLS and ULS analysis is assessed for the spar-buoy turbine by considering the same DLCs as for the monopile turbine (listed in Table 4). Only a different water depth (320 m) is considered for the spar-buoy turbine.

4.3.1 | Spar-buoy turbine FLS analysis

Following the same procedure as outlined in Section 4.2.1, FLS analysis results of the spar-buoy turbine are obtained and listed in Table 7. The aggregated DELs with the same Weibull distribution are also calculated. Simulation results of the wind turbine responses when subjected to an average wind speed of 16 m/s are illustrated in Figure 14. The PSD of the tower top displacement in the fore-aft, side-to-side directions, and platform pitch movement are shown in Figure 14A,D,G, with the same window number as the one used in the monopile turbine FLS analysis. Their corresponding time domain responses are shown in Figure 14B,E,H. Narrowed time window responses are also shown in Figure 14C,G,I. Again, only responses with the TMD and IBA$_{6E3}$ are illustrated in the figures due to the moderate performance improvements of the IBA$_{6E3}$ compared with IBA$_{4E1}$.

It can be seen that IBAs have the ability to further suppress the tower bending mode of the spar-buoy turbine at around 0.5 Hz. Similarly, IBAs are more effective in the side-to-side direction where the improvement can be up to 3.3%, as there is little aerodynamic damping in this direction. However, the platform pitch mode (around 0.035 Hz) is not effectively suppressed regardless of either a TMD or an IBA is employed. Therefore, the platform pitch angle is unaltered. The peak in Figure 14A, at around 0.15 Hz, is the spectrum of the wave load. This is not observed

TABLE 7 Spar-buoy turbine FLS analysis results

	Fore-aft tower base fatigue load (kNm)		Side-to-side tower base fatigue load (kNm)			
Wind speed	TMD	IBA_{4E1}	IBA_{6E3}	TMD	IBA_{4E1}	IBA_{6E3}
4	4,569	4,555	4,525	186.3	178.8	175.8
8	8,597	8,568	8,559	659.3	644.0	642.9
12	12,861	12,761	12,808	838.3	821.5	821.1
16	14,006	13,836	13,927	1,457	1,405	1,404
20	23,563	23,373	23,440	2,526	2,362	2,366
24	18,636	18,558	18,493	3,848	3,720	3,717
Aggregated	488,022	484,764	485,458	38,249	37,037	36,979
Improvements	-	0.7%	0.5%	-	3.2%	3.3%

Abbreviations: FLS, fatigue limit state; IBA, inerter-based absorber; TMD, tuned mass damper.

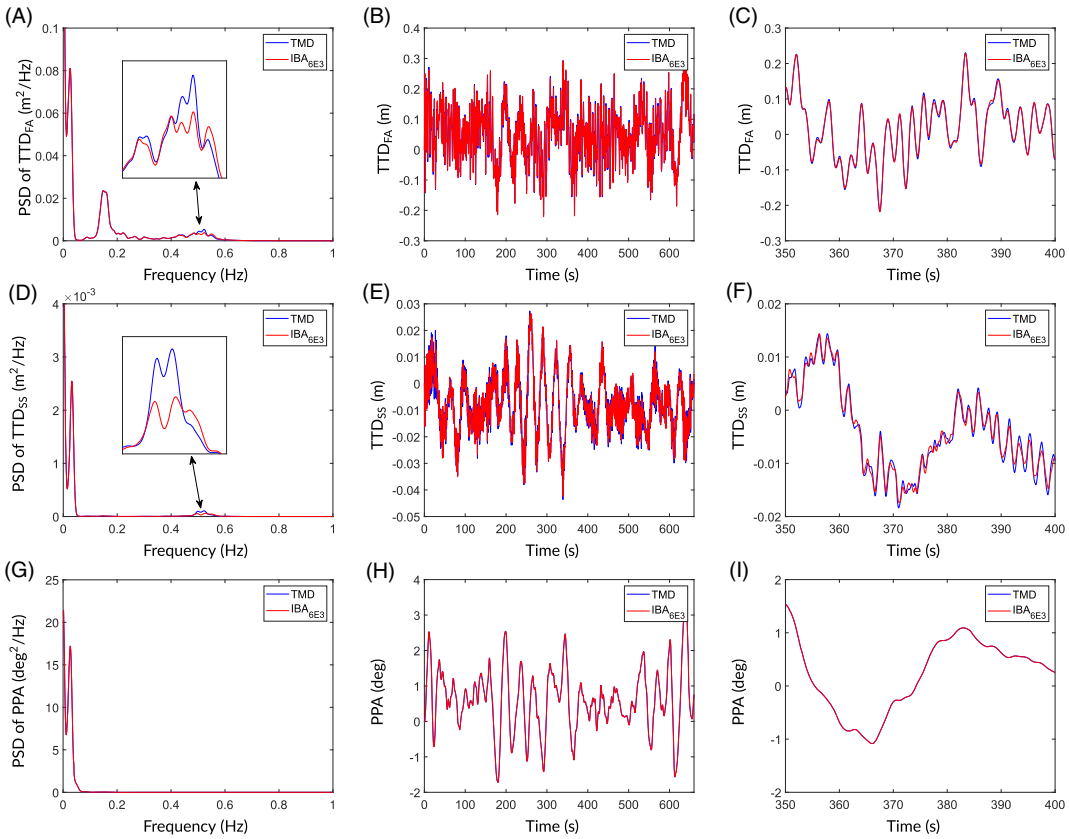

FIGURE 14 Frequency domain responses (left), time domain responses (middle), and narrowed time windows responses (right) of the spar-buoy turbine under design load case (DLC) 1.2 (16 m/s wind speed) with the tower top displacement (TTD) in the fore-aft (FA) direction (A, B, C), in the side-to-side (SS) direction (D, E, D), and with the platform pitch angle (PPA) (G, H, I) [Colour figure can be viewed at wileyonlinelibrary.com]

in the side-to-side direction as the wind and wave loads are always considered aligned. The stroke is also investigated under the FLS analysis. For the TMD, the maximum stroke under 24 m/s wind speed is 0.62 m in the fore-aft direction and 0.13 m in the side-to-side direction. While for the IBA_{4E1} and IBA_{6E3}, the maximum stroke is 0.71 and 0.74 m in the fore-aft direction and 0.13 and 0.13 m in the side-to-side direction, respectively. It can be seen that the stroke of the IBAs are slightly larger than the TMD, but it is still within the space limit of the turbine nacelle. Again, in order to achieve a similar performance as the optimum TMD, the $IBA_{6E3}$with a reduced mass values of 7,680 kg is also verified with slightly better performance than the TMD in both the fore-aft and side-to-side directions. This demonstrates the identified IBA has practical advantages for the offshore wind turbine applications compared with the TMD.

TABLE 8 Spar-buoy turbine ULS analysis results

Evaluation type	Evaluation index	TMD	IBA_{4E1} (Imp.)	IBA_{6E3} (Imp.)
	Max TTD fore-aft (m)	0.576	0.576 (0%)	0.576 (0%)
	Max TTD side-side (m)	0.401	0.398 (0.9%)	0.411 (-2.4%)
Time domain responses				
	Max tower bending moment fore-aft (kN·m)	119,205	119,115 (0%)	119,117 (0%)
	Max tower bending moment side-side (kN·m)	78,113	77,034 (1.4%)	78,395 (-0.3%)
	Amplitude TTD fore-aft (m^2/Hz)	0.00129	0.00126 (2.5%)	0.00122 (6.1%)
PSD of the responses	Amplitude TTD side-side (m^2/Hz)	0.0203	0.0129 (18.7%)	0.0123 (20.1%)
(between 0.4 and 0.6 Hz)	Amplitude tower bending moment fore-aft ((kN·m)^2/Hz)	4.04×10^7	3.90×10^7 (3.4%)	3.76×10^7 (6.9%)
	Amplitude tower bending moment side-side ((kN·m)^2/Hz)	6.66×10^8	4.22×10^8 (36.6%)	4.01×10^8 (39.7%)

Abbreviations: IBA, inerter-based absorber; TMD, tuned mass damper; TTD, tower top displacement; ULS, ultimate limit state.

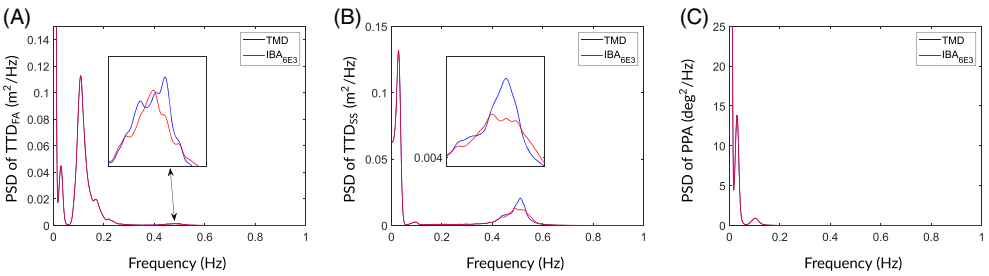

FIGURE 15 Frequency responses of the spar-buoy turbine under DLC 6.1a with the tower top displacement (TTD) (A) in the fore-aft (FA) direction, (B) in the side-to-side (SS) direction, and (C) with the platform pitch angle (PPA) [Colour figure can be viewed at wileyonlinelibrary.com]

4.3.2 | Spar-buoy turbine ULS analysis

Simulations with DLC 6.1a are performed for the spar-buoy turbine, where the performance indices are defined as the absolute maximum tower top displacement and tower base bending moment of each simulation averaged over six different random simulations. The amplitude of the tower top displacement and tower base bending moment in the frequency domain around the tower bending mode (between 0.4 and 0.6 Hz) are also included for comparison. Results are shown in Table 8, where improvements in the time domain with up to 1.4% are obtained. Moreover, improvements in the frequency domain can be up to 6.9% and 39.7% in the fore-aft and side-to-side direction, respectively. The PSD calculated by *pwelch* with 36 windows for one of the ULS simulation results is shown in Figure 15A-C, which are the tower fore-aft, side-to-side responses, and the platform pitch movement, respectively. It can be observed that the IBA_{6E3} is effective for the tower bending mode around 0.5 Hz under extreme load case. However, the platform pitch mode is dominant in both the fore-aft and side-to-side directions at around 0.035 Hz. This phenomenon perhaps explains why the improvement of the maximum tower fore-aft and side-to-side displacements under ULS is less significant. Moreover, the load spectrum is dominant in the fore-aft direction at around 0.1 Hz and is not effectively suppressed (as shown in Figure 15A), hence the performance is less significant in this direction even though the blades are all feathered.

5 | CONCLUSIONS

In this paper, IBAs are adopted to reduce the tower vibrations of a fix-bottom and a floating offshore wind turbine. A newly developed structure-immittance approach is employed to identify the beneficial IBA configurations with no more than six spring-damper-inerter elements. First, simplified linear wind turbine models are established based on their corresponding OpenFAST models. Then, optimisations to reduce the tower top displacements are conducted. In order to assess their performance in realistic conditions, OpenFAST is modified to be able to include the transfer functions of any IBAs. Therefore, both the benefical IBA identification approach—the structure-immittance approach, and the simulation tool—the modified OpenFAST, can include a whole range of absorbers. This enables the full investigation of generalised absorber configurations applied on various turbine systems. In this study, by employing the identified optimal IBAs, the monopile and spar-buoy turbines are simulated under different wind and wave conditions, including normal operational condition (corresponding to the FLS) and extreme load condition (corresponding to the ULS) with the the conventional vibration absorber, the TMD, as a benchmark. Results are obtained and concluded as follows:

1 The structure-immittance approach has the ability of obtaining all possible beneficial configurations across a whole range of IBA candidates; therefore, the structure-based IBAs, which has been previously proposed and proved to be effective for the offshore wind turbine systems, can be regarded as a subset of the IBAs identified by the structure-immittance approach. Based on the established linear monopile and spar-buoy turbine models, it is shown that no 3-element IBA could provide better performance than the TMD, and all 5-element candidates containing two springs, two dampers, and one inerter cannot provide extra benefits over four elements IBAs. For the 4-element and 6-element IBA candidates, four IBAs for each case are identified, which can provide equivalent performance improvements. This expands the design options for the practical implementation of IBAs. Optimisation results show that up to 7.3% and 6.4% performance improvements can be obtained by employing the linear monopile and spar-buoy turbine models, respectively.
2 Under realistic metocean external conditions simulated in OpenFAST, the identified IBAs show performance improvements compared to the TMD for the FLS analysis, where the tower DEL can be reduced up to 5.8% and 3.3% for the monopile and the spar-buoy turbines, respectively. The reduction of DEL is larger in the side-to-side direction as there is less aerodynamic damping in this direction. The reason that the reduction for the spar-buoy turbine is smaller than that for the monopile one is that the identified IBAs only tuned the tower fore-aft mode of the spar-buoy turbine, while the platform pitch mode is not effectively suppressed.
3 The identified IBAs also show performance improvements compared with the TMD under the ULS analysis. In the time domain, the maximum tower base bending moment is reduced up to 2.4% and 1.4% for the monopile and the spar-buoy turbines, respectively. In the frequency domain, the amplitude of the tower bending mode can be reduced up to 37.0% and 39.7% correspondingly.
4 Compared with the relatively modest performance improvements using IBAs, mass value of the optimum IBAs for the monopile and spar-buoy turbines can be reduced by 25.1% (7,486 kg) and 23.2% (76,80 kg), respectively, to achieve the same performance as the optimum TMD. This is crucial for the utilisation of IBAs in offshore wind turbine vibration mitigation applications, where the total mass added on the nacelle can be substantially reduced.

ACKNOWLEDGEMENTS

The authors would like to acknowledge the support of the Engineering and Physical Sciences Research Council (EPSRC), the China Scholarship Council, the University of Bristol and Atkins: Y.-Y.Li is funded by the University of Bristol and the China Scholarship Council; J.Z.Jiang is supported by the EPSRC with Grant NumberEP/P013546/1 and by Atkins with the Impact Acceleration Account Award. The authors would also like to express their special gratitude to Prof. John Macdonald for his precious advices on this paper.

FINANCIAL DISCLOSURE

None reported.

CONFLICTS OF INTEREST

The authors declare no potential conflict of interests.

ORCID

Semyung Park https://orcid.org/0000-0002-7083-2035
Jason Zheng Jiang https://orcid.org/0000-0002-9059-7984

REFERENCES

1. Musial W, Butterfield S, Ram B. Energy from offshore wind. In: Offshore Technology Conference; 2006; Houston, TX.
2. Frahm H. Device for damping vibrations of bodies. US Patent 1911. No. 989958.
3. Den Hartog JP. *Mechanical Vibrations*. New York: McGraw-Hill; 1956. 4th Ed.
4. Murtagh P, Ghosh A, Basu B, Broderick B. Passive control of wind turbine vibrations including blade/tower interaction and rotationally sampled turbulence. *Wind Energy*. 2008;11:305-317.
5. Lackner M, Rotea M. Passive structural control of offshore wind turbines. *Wind Energy*. 2011;14(3):373-388.
6. Jonkman J, Buhl M. *FAST UserÑs Guide. Tech. Rep. TP-500-38230*, National Renewable Energy Laboratory. Colorado: Golden; 2011.
7. Stewart G, Lackner M. Offshore wind turbine load reduction employing optimal passive tuned mass damping systems. *IEEE Trans Cont Syst Tech*. 2013;21(4):1090-1104.
8. Stewart G, Lackner M. The impact of passive tuned mass dampers and wind-wave misalignment on offshore wind turbine loads. *Eng Struct*. 2014;73:54-61.
9. Si Y, Karimi H, Gao H. Modelling and optimization of a passive structural control design for a spar-type floating wind turbine. *Eng Struct*. 2014;69:168-182.
10. Zuo H, Bi K, Hao H. Using multiple tuned mass dampers to control offshore wind turbine vibrations under multiple hazards. *Eng Struct*. 2017;141:303-315.
11. Sun C. Semi-active control of monopile offshore wind turbines multi-hazards. *Mech Syst Sig Proc*. 2018;73:54-61.
12. Park S, Lackner M, Pourazarm P, Rodriguez Tsouroukdissian A, Cross-Whiter J. An investigation on the impacts of passive and semiactive structural control on a fixed bottom and a floating offshore wind turbine. *Wind Energy*. 2019;22(11):1451-1471.

13. Smith MC. Synthesis of mechanical networks: the inerter. *IEEE Trans Auto Cont*. 2002;47(10):1648-1662.
14. Firstone FA. A new analogy between mechanical and electrical systems. *The J Acoust Soc America*. 1933;4(3):249-267.
15. Papageorgiou C, Smith M. Positive real synthesis using matrix inequalities for mechanical networks: application to vehicle suspension. *IEEE Trans Cont Syst Tech*. 2006;14:423-435.
16. Smith M, Wang FC. Performance benefits in passive vehicle suspensions employing inerters. *Vehicle Syst Dyn*. 2004;42:235-247.
17. Wang FC, Liao MK, Liao BH, Su WJ, Chan HA. The performance improvements of train suspension systems with mechanical networks employing inerters. *Vehicle Syst Dyn*. 2009;47:805-830.
18. Jiang JZ, Matamoros-Sanchez A, Goodall R, Smith M. Passive suspensions incorporating inerters for railway vehicles. *Vehicle Syst Dyn*. 2011;50: 263-276.
19. Wang FC, Hsieh MR, Chen HJ. Stability and performance analysis of a full-train system with inerters. *Vehicle Syst Dyn*. 2012;50:545-571.
20. Li Y, Jiang JZ, Neild NA. Inerter-based configurations for main-landing-gear shimmy suppression. *J Aircraft*. 2014;54:684-693.
21. Zhang SY, Jiang JZ, Neild SA. Optimal configurations for a linear vibration suppression device in a multi-storey building. *Struct Cont Health Mon*. 2016; 24(3). https://doi.org/10.1002/stc.1887
22. Ikago K, Saito K, Inoue N. Seismic control of single–degree–of–freedom structure using tuned viscous mass damper. *Earthquake Eng Struct Dyn*. 2012; 41(3):453-474.
23. IkagoK, Sugimura Y, Saito K, Inoue N. Modal Response Characteristics of a Multiple-Degree-Of-Freedom Structure Incorporated with Tuned Viscous Mass Dampers. *Journal of Asian Architecture and Building Engineering*. 2012;11(2):375–382. http://dx.doi.org/10.3130/jaabe.11.375
24. Swift SJ, Smith MC, Glover AR, Papageorgiou C, Gartner B, Houghton NE. Design and modelling of a fluid inerter. *Int J Cont*. 2013;86(11):2035-2051.
25. Liu X, Titurus B, Jiang JZ, Harrison A. Model identification methodology for fluid-based inerters. *Mech Syst Signal Proc*. 2018;106:479-494.
26. Liu X, Titurus B, Jiang JZ. Generalisable model development for fluid-inerter integrated damping devices. *Mech Mach Theo*. 2019;137:1-22.
27. Hu Y, Wang J, Chen M, Li Z, Sun Y. Load mitigation for a barge-type floating offshore wind turbine via inerter-based passive structural control. *Eng Struct*. 2018;177:198-209.
28. Zhang R, Zhao Z, Dai K. Seismic response mitigation of a wind turbine tower using a tuned parallel inerter mass system. *Eng Struct*. 2019;180:29-39.
29. Marian L, Giaralis A. Optimal design of a novel tuned mass-damper-inerter (TMDI) passive vibration control configuration for stochastically support-excited structural systems. *Prob Eng Mech*. 2014;38:156-164.
30. SarKar S, Fitzgerald B. Vibration control of spar-type floating offshore wind turbine towers using a tuned mass-damper-inerter. *Struct Cont Health Mon*. 2019;27(1):https://doi.org/10.1002/stc.2471
31. Zhang SY, Jiang JZ, Neild NA. Passive vibration control: a structure-immittance approach. *Proc Royal Soc A*. 2017;21(4):1090-1104.
32. https://openfast.readthedocs.io/en/master.
33. Jonkman J, Butterfield S, Musial W, Scott G. *Definition of a 5-MW reference wind turbine for offshore system development. Tech. Rep. Technical Report NREL/TP-500-38060*, National Renewable Energy Laboratory. Colorado: Golden; 2009.
34. Jonkman J, Musial W. *Offshore code comparison collaboration (OC3) for IEA Task 23 offshore wind technology and deployment. Tech. Rep. Technical Report NREL/TP-5000-48191*, National Renewable Energy Laboratory. Colorado: Golden; 2010.
35. Jonkman J, Butterfield S, Passon P, et al. *Offshore code comparison collaboration within IEA Wind Annex XXIII: Phase II Results regarding monopile foundation modeling. Tech. Rep. Technical Report NREL/TP-500-42471*, National Renewable Energy Laboratory. Colorado: Golden; 2008.
36. Jonkman J. *Definition of the Floating System for Phase IV of OC3. Tech. Rep. Technical Report NREL/TP-500-47535*, National Renewable Energy Laboratory. Colorado: Golden; 2010.
37. Høgsberg J. Vibration control by piezoelectric proof-mass absorber with resistive-inductive shunt. *Mech Adv Mat Struct*. 2019;1–13. https://doi.org/10.1080/15376494.2018.1551587
38. Krenk S. Frequency analysis of the tuned mass damper. *J Appl Mech*. 2005;72(6):936-942.
39. Kuo F. *Network analysis and synthesis*, 2nd Ed: John Wiley and Sons; 1962.
40. Fischer T, Vries dW, Schmidt B. *UpWind Design Basis (WP4: offshore foundation and support structures)*, tech. rep. 70550 Stuttgart, Germany: University of Stuttgart; Allmandring 5B; 2010.
41. TC88 I. *Design requirements for offshore wind turbines. Tech. Rep. IEC 61400-3*. 70550 Stuttgart, Germany: International Electrotechnial Commission; Allmandring 5B; 2009.
42. Haid L, Stewart G, Jonkman J, Robertson A, Lackner M, Matha D. *Simulation-length requirements in the loads analysis of offshore floating wind turbines*, Tech. Rep. NREL/CP-5000-58153. Golden, Colorado: National Renewable Energy Laboratory; 2013.
43. Hayman G. Mlife theory manual for version 1.00. tech. rep., Golden, Colorado, National Renewable Energy Laboratory; 2012.
44. La Cava W, Lackner M. *Theory manual for the Tuned Mass Damper Module in FAST v8*. MA, USA: University of Massachusetts Amherst: Amherst; 2015. https://nwtc.nrel.gov/system/files/TMD_theory_manual.pdf

How to cite this article: Li Y-Y, Park S, Jiang JZ, Lackner M, Neild S, Ward I. Vibration suppression for monopile and spar-buoy offshore wind turbines using the structure-immittance approach. *Wind Energy*. 2020;23:1966–1985. https://doi.org/10.1002/we.2544

APPENDIX A: IMPLEMENTATION OF INERTER-BASED ABSORBERS IN OPENFAST

Considering the equation of motion of an inerter-based absorber (IBA) in the *X* direction based on the previous study done by La Cava and Lackner[44] as follows:

$$m_X\ddot{x}_{IBA_X/P} - m_X\left(\dot{\varphi}_P^2 + \dot{\psi}_P^2\right)x_{IBA_X/P} + \mathcal{L}^{-1}(Y'(s))\ddot{x}_{IBA_X/P} = m_X a_{G_X/O} + (F_{ext_X} + F_{StopFrc_X}) - m_X\ddot{x}_{P/O}, \tag{A1}$$

where m_X is the mass value of an absorber in *X* direction. Subscripts *O*, *P*, and *IBA* represent the origin point of the global inertial reference frame, the origin point of the noninertial reference frame fixed to the tower top where IBAs are at rest, and the origin point of an IBA, respectively. $x_{IBA_X/P}$ is the displacement of an IBA relative to the tower top non-inertial reference frame origin point *IBA*. a_G is the gravity acceleration. Now setting

$$\mathbf{B}_X u_X = m_X a_{G_X/O} + (F_{ext_X} + F_{StopFrc_X}) - m_X\ddot{x}_{P/O}, \tag{A2}$$

where u_X is the input vector with input matrix denoted by $\mathbf{B}_X$. Note that $\mathcal{L}^{-1}(Y'(s))\ddot{x}_{IBA_X/P}$ is the output force F_f generated between the two terminals of the network, where the *x* in equation (12) is the $x_{IBA_X/P}$ in equation (A1. Therefore, equation (A1) can be rewritten as follows:

$$m_X\ddot{x}_{IBA_X/P} - m_X\left(\dot{\varphi}_P^2 + \dot{\psi}_P^2\right)x_{IBA_X/P} + F_f = \mathbf{B}_X u_X. \tag{A3}$$

Integrate equation (12) on both sides considering all variables with zero initial condition, and substitute it into equation (A3).

$$m_X\ddot{x}_{IBA_X/P} - m_X\left(\dot{\varphi}_P^2 + \dot{\psi}_P^2\right)x_{IBA_X/P} + \mathbf{c}_1\left(\mathbf{A}_1\int\boldsymbol{\omega}_f + \mathbf{b}_1\dot{x}_{IBA_X/P}\right) + d_1\ddot{x}_{IBA_X/P} = \mathbf{B}_X u_X. \tag{A4}$$

Then, the equation of motion can be reformulated by grouping orders of $x_{IBA_X/P}$ as follows:

$$M_X\ddot{x}_{IBA_X/P} + C_X\dot{x}_{IBA_X/P} + K_X x_{IBA_X/P} + \mathbf{c}_1\mathbf{A}_1\int\boldsymbol{\omega}_f = \mathbf{B}_X u_X, \tag{A5}$$

where

$$\begin{aligned} M_X &= m_X + d_1 \\ C_X &= \mathbf{c}_1\mathbf{b}_1 \\ K_X &= -m_X(\dot{\varphi}_P^2 + \dot{\psi}_P^2). \end{aligned}$$

Combining the absorber's mass states *x* with its ficitious states $\int\boldsymbol{\omega}_f$, the entire system can now be written in the state-space form in the time domain as follows:

$$\dot{x}_{w_X} = \mathbf{A}_{ss_X}x_{w_X} + \mathbf{B}_{ss_X}u_X \tag{A6}$$

with

$$x_{w_X} = \begin{bmatrix} \dot{x}_{IBA_X/P} \\ x_{IBA_X/P} \\ \int\boldsymbol{\omega}_f \end{bmatrix}, \mathbf{A}_{ss_X} = \begin{bmatrix} -M_X^{-1}C_X & -M_X^{-1}K_X & -M_X^{-1}\mathbf{c}_1\mathbf{A}_1 \\ 1 & 0 & \mathbf{0} \\ \mathbf{b}_1 & \mathbf{0} & \mathbf{A}_1 \end{bmatrix}, \mathbf{B}_{ss_X} = \begin{bmatrix} M_X^{-1}\mathbf{B}_X \\ \mathbf{0}_{(N+1)\times 1} \end{bmatrix}.$$

N is the dimension of the fictitious states. Therefore, with the zero initial condition, the force exerted by the IBA in *X* direction (i.e., equation (11)) can be reformed as follows:

$$F_{f_X} = \mathbf{c}_1 \left(\mathbf{A}_1 \int \boldsymbol{\omega}_f + \mathbf{b}_1 \dot{x}_{IBA_X/P} \right) + d_1 \ddot{x}_{IBA_X/P}. \tag{A7}$$

Similarly, for an IBA in the *Y* direction, the state space equation and the force expression are obtained as follows:

$$\dot{x}_{w_Y} = \mathbf{A}_{ss_Y} x_{w_Y} + \mathbf{B}_{ss_Y} u_Y \tag{A8}$$

and

$$F_{f_Y} = \mathbf{c}_1 \left(\mathbf{A}_1 \int \boldsymbol{\omega}_f + \mathbf{b}_1 \dot{x}_{IBA_Y/P} \right) + d_1 \ddot{x}_{IBA_Y/P}, \tag{A9}$$

where

$$x_{w_Y} = \begin{bmatrix} \dot{x}_{TMD_Y/P} \\ x_{TMD_Y/P} \\ \int \boldsymbol{\omega}_f \end{bmatrix}, \mathbf{A}_{ss_Y} = \begin{bmatrix} -M_Y^{-1} C_Y & -M_Y^{-1} K_Y & -M_Y^{-1} \mathbf{c}_1 \mathbf{A}_1 \\ 1 & 0 & \mathbf{0} \\ \mathbf{b}_1 & \mathbf{0} & \mathbf{A}_1 \end{bmatrix}, \mathbf{B}_{ss_Y} = \begin{bmatrix} M_Y^{-1} \mathbf{B}_Y \\ \mathbf{0}_{(N+1)\times 1} \end{bmatrix}$$

and

$$M_Y = m_Y + d_1,\ C_Y = \mathbf{c}_1 \mathbf{b}_1,\ K_Y = -m_Y (\dot{\theta}_P^2 + \dot{\psi}_P^2).$$

Hence, by implementing equation (A6) to (A9) into the IBA module, transfer functions of different IBAs can be included in OpenFAST.